

Original citation:

Bzdek, Bryan, Collard, Liam, Sprittles, James E., Hudson, Andrew and Reid, Jonathan. (2016) Dynamic measurements and simulations of airborne picolitre-droplet coalescence in holographic optical tweezers. *Journal of Chemical Physics*, 145 (5). 054502.

Permanent WRAP URL:

<http://wrap.warwick.ac.uk/80437>

Copyright and reuse:

The Warwick Research Archive Portal (WRAP) makes this work of researchers of the University of Warwick available open access under the following conditions.

This article is made available under the Creative Commons Attribution 4.0 International license (CC BY 4.0) and may be reused according to the conditions of the license. For more details see: <http://creativecommons.org/licenses/by/4.0/>

A note on versions:

The version presented in WRAP is the published version, or, version of record, and may be cited as it appears here.

For more information, please contact the WRAP Team at: wrap@warwick.ac.uk

Dynamic measurements and simulations of airborne picolitre-droplet coalescence in holographic optical tweezers

Bryan R. Bzdek, Liam Collard, James E. Sprittles, Andrew J. Hudson, and Jonathan P. Reid^{*}

Citation: [The Journal of Chemical Physics](#) **145**, 054502 (2016); doi: 10.1063/1.4959901

View online: <http://dx.doi.org/10.1063/1.4959901>

View Table of Contents: <http://aip.scitation.org/toc/jcp/145/5>

Published by the [American Institute of Physics](#)

Articles you may be interested in

[Coalescence of liquid drops: Different models versus experiment](#)

[The Journal of Chemical Physics](#) **24**, 122105 (2012); doi: 10.1063/1.4773067



**COMPLETELY
REDESIGNED!**

Physics Today Buyer's Guide
Search with a purpose.

Dynamic measurements and simulations of airborne picolitre-droplet coalescence in holographic optical tweezers

Bryan R. Bzdek,¹ Liam Collard,² James E. Sprittles,³ Andrew J. Hudson,⁴ and Jonathan P. Reid^{1,a)}

¹*School of Chemistry, University of Bristol, Bristol BS8 1TS, United Kingdom*

²*Department of Mathematics, University of Leicester, Leicester LE1 7RH, United Kingdom*

³*Mathematics Institute, University of Warwick, Coventry CV4 7AL, United Kingdom*

⁴*Department of Chemistry, University of Leicester, Leicester LE1 7RH, United Kingdom*

(Received 3 March 2016; accepted 14 July 2016; published online 1 August 2016)

We report studies of the coalescence of pairs of picolitre aerosol droplets manipulated with holographic optical tweezers, probing the shape relaxation dynamics following coalescence by simultaneously monitoring the intensity of elastic backscattered light (EBL) from the trapping laser beam (time resolution on the order of 100 ns) while recording high frame rate camera images (time resolution $<10\ \mu\text{s}$). The goals of this work are to: resolve the dynamics of droplet coalescence in holographic optical traps; assign the origin of key features in the time-dependent EBL intensity; and validate the use of the EBL alone to precisely determine droplet surface tension and viscosity. For low viscosity droplets, two sequential processes are evident: binary coalescence first results from the overlap of the optical traps on the time scale of microseconds followed by the recapture of the composite droplet in an optical trap on the time scale of milliseconds. As droplet viscosity increases, the relaxation in droplet shape eventually occurs on the same time scale as recapture, resulting in a convoluted evolution of the EBL intensity that inhibits quantitative determination of the relaxation time scale. Droplet coalescence was simulated using a computational framework to validate both experimental approaches. The results indicate that time-dependent monitoring of droplet shape from the EBL intensity allows for robust determination of properties such as surface tension and viscosity. Finally, the potential of high frame rate imaging to examine the coalescence of dissimilar viscosity droplets is discussed. © 2016 Author(s). All article content, except where otherwise noted, is licensed under a Creative Commons Attribution (CC BY) license (<http://creativecommons.org/licenses/by/4.0/>). [<http://dx.doi.org/10.1063/1.4959901>]

I. INTRODUCTION

The coalescence of airborne droplets is relevant to a number of important research areas, including cloud dynamics,^{1,2} aerosol mixing state³ and lifetime,⁴ inkjet printing,⁵ spray drying,⁶ and intranasal drug delivery.⁷ However, the experimental investigation of droplet coalescence is challenging for two reasons. First, the size of the coalescing droplets relevant to these processes is typically small, on the order of nanometres to micrometres. Second, the time scales governing coalescence are also typically short, on the order of tens of microseconds or less for low viscosity droplets in the relevant size range. Understanding the dynamic factors that determine the outcome of a binary coalescence event, influencing the coalescence kernel, relaxation, morphology, and heterogeneity of the final particle, requires detailed knowledge of relative trajectories and physicochemical properties of the approaching droplets. In particular, fundamental droplet properties such as surface tension,^{8–10} viscosity,¹¹ density, interparticle interactions (attractions and repulsions),^{12,13} internal structure,^{14,15} and fluid

flows¹⁶ are critical to understand the details of the coalescence process.

There are a number of methods available to study the binary coalescence of droplets. The most common method is to use brightfield microscopy coupled with a camera to capture images during the coalescence. For droplets with radii on the order of millimetres, an imaging frequency (frame rate) on the order of 10 kHz is required to study coalescence.^{9,17–19} If one wishes to study much smaller droplets relevant to processes like cloud formation (where radii are on the order of micrometres or smaller), the required time resolution must be a few microseconds or lower.^{8,10} Illumination of the coalescence event to obtain a clear contrast of the droplets in video images becomes increasingly challenging at microsecond exposure times. In addition, high-speed cameras capable of recording sequences of images at MHz frame rates are expensive. An alternative method to obtain high quality images of droplet shapes with fast time resolution and good phase contrast is by polychromatic hard X-rays.²⁰ Fezzaa and Wang demonstrated the use of ultrafast X-ray phase contrast to study the dynamics of two coalescing droplets in air with images exposed for 472 ns and acquired in 3.6 μs intervals.²¹ However, this method also requires a high-speed camera as well as X-rays from a synchrotron. An electrical measurement of the resistance and

^{a)} Author to whom correspondence should be addressed. Electronic mail: j.p.reid@bristol.ac.uk.

capacitance of dilute water-glycerol droplets containing salt during coalescence has been shown to indirectly provide detail about time-dependent processes.^{22,23} This approach can give a time resolution as fast as 10 ns but requires that the droplets be anchored to separate nozzles rather than freely suspended in air. Indeed, all of the approaches discussed above examine droplets supported by a substrate.²⁴ Kohno and co-workers have developed a method to study the collisions of droplets tens of micrometres in radius pulsed from opposing piezo-driven nozzles.²⁵ By this method, they have determined chemical reaction rates upon collision of two droplets with different compositions²⁶ and investigated shape deformations upon collision.²⁷

In previous work, we have captured two or more airborne droplets with radii 6–10 μm (corresponding to volumes of just 1–4 pL) using optical tweezers.^{8,11,28–35} The relative positions of a pair of droplets can be controlled by a holographic system through the relative positions of the two optical traps.^{8,11} In order to study the coalescence event, the intensity of elastic backscattered light (EBL) from the optical tweezers was recorded on a fast photodiode connected to an oscilloscope, permitting indirect determination of changes in droplet shape and position with a time resolution of order 100 ns. The time dependence of the EBL takes the form of a damped oscillator during the relaxation of the composite droplet. Although this approach enables precise, quantitative determination of both the surface tension and viscosity of the final droplet,^{8,11} the EBL is a complex signal with many features arising during the course of the coalescence event which lead to ambiguity in interpretation of the temporal dependence.

The goals of this work are to examine the coalescence of airborne picolitre-volume droplets across a range of viscosities and to correlate the EBL with video images recorded by a high frame rate camera. The combination of high frame rate imaging and EBL enables the study of the dynamics of coalescence, unambiguous determination of the origin of key EBL features, and validation of the use of the EBL alone to precisely determine droplet surface tension and viscosity. The impact of experimental variables such as coalescence geometry on EBL is determined. Moreover, simulations of droplet coalescence are performed in order to corroborate interpretations of both EBL intensity and high frame rate images. Finally, we discuss the potential of high frame rate imaging to study the coalescence of two droplets of dissimilar viscosity, an experiment that would be inaccessible to the EBL alone in future studies. The combination of direct and indirect imaging modalities along with theoretical simulation demonstrates that holographic optical tweezers can provide robust and relatively straightforward determinations of fundamental droplet properties such as surface tension and viscosity in size ranges relevant to atmospheric and industrial processes.

II. EXPERIMENTAL AND THEORETICAL METHODS

A. Holographic optical trapping and imaging

The holographic optical tweezers setup used in this work has been described in detail previously.^{13,28} The

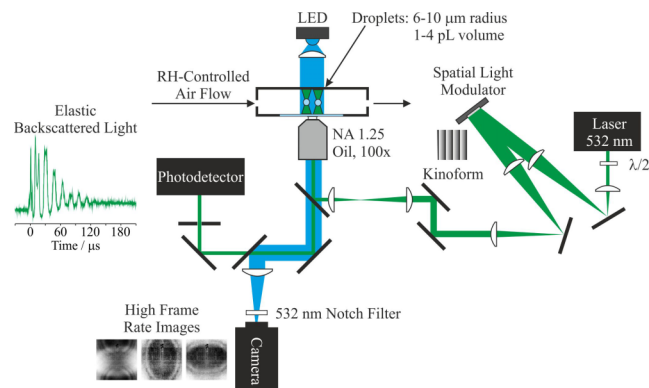


FIG. 1. Schematic description of the experimental setup. 532 nm laser light is dynamically shaped by a liquid crystal on silicon spatial light modulator to create two optical traps whose relative positions can be adjusted. Elastic backscattered light (EBL) is directed to a photodetector and recorded by an oscilloscope. Brightfield illumination is accomplished with a blue LED and is directed to a high frame rate camera.

experimental apparatus and a few significant differences to previous work, including the addition of a high frame rate camera, are described below. The experimental setup used here is illustrated in Fig. 1. In the experiment, the optical tweezers were configured in the inverted microscope geometry. Multiple, steerable optical traps were formed by dynamically shaping the phase front of a continuous wave 532 nm laser (Laser Quantum, Opus 3QW) using a liquid crystal on silicon spatial light modulator (LCOS-SLM, Hamamatsu X10468). The beam was expanded to fill the SLM display, which was conjugated to the back focal plane of a high numerical aperture microscope objective (Olympus ACH, 100 \times /1.25 oil) by a pair of condensing 4 f telescopes. The separation between the two optical traps was controlled through a pre-calculated sequence of kinoforms (phase-only computer generated holograms). The rate at which the kinoforms (and, therefore, trap separation) is changed is user-controlled. Eventually, the trap separation became sufficiently small that the droplets coalesced. The relative laser power in each trap was controlled by a half-wave plate located before the SLM.

The important change to the experimental setup relative to that used in the past^{8,11,28} was the integration of a high frame rate camera (Vision Research, Phantom v.7.3), which can acquire images at frame rates better than 120 kHz. The droplets were illuminated with a high power light-emitting diode (LED) (Thorlabs, 470 nm). Additionally, the EBL (532 nm) was collected using a silicon photodetector (Thorlabs, DET 110) and recorded using a low-load, 12 bit analog-to-digital converter (ADC) resolution, 2.5 GS⁻¹ sample rate oscilloscope (LeCroy, HDO 6034-MS). The oscilloscope was triggered at the onset of coalescence of two trapped droplets when EBL intensity surpassed a threshold value, thereby recording the full profile of intensity around this time. In all experiments, the high frame rate camera was triggered synchronously with the oscilloscope. In this way, the camera images and EBL could be directly compared. Due to space constraints, installation of the high frame rate camera into the setup prevented the acquisition of parallel Raman spectra, which would have allowed for accurate determination

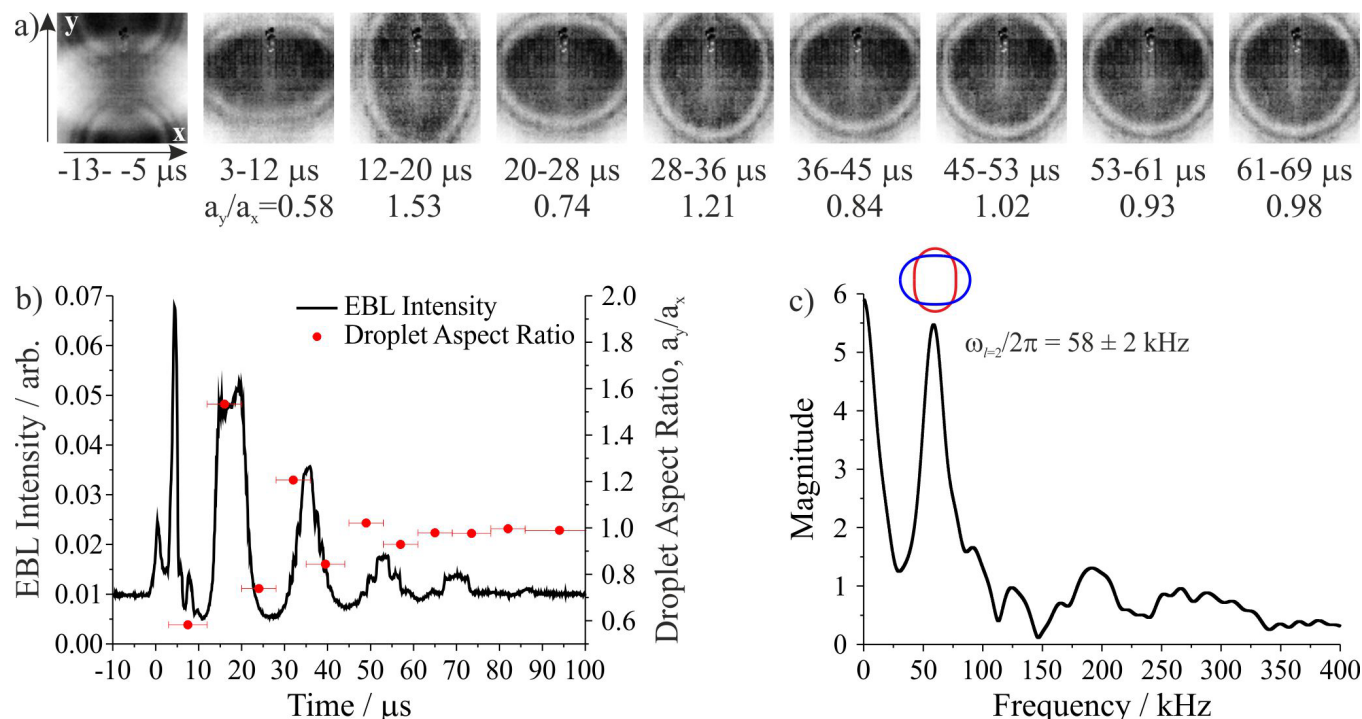


FIG. 2. Coalescence along an axis transverse to the trapping beam of two sodium chloride droplets doped with the surfactant sodium dodecyl sulfate. (a) High frame rate camera images of the coalescence event. Time ranges underneath each image provide the exposure period during which the image was taken. Aspect ratios are also reported for each image after the coalescence time. (b) EBL collected after coalescence (left axis, time $t = 0$ corresponds to the moment of coalescence) and droplet aspect ratios (a_y/a_x) determined from high frame rate imaging (right axis). (c) Fast Fourier transform of the EBL gives the frequency of the shape oscillation.

of droplet size, refractive index, and wavelength dispersion as in previous work. In practice, these properties were not necessary for the interpretation of the experiments described here.

High frame rate images recorded by the camera were sent to a computer operating the Phantom PCC 2.2 software package. Images were collected, and the contrast of these images was enhanced using the ImageJ software package (v.1.46r, <http://imagej.nih.gov/ij/>) in order to more clearly show the position and shape of the droplets. No other image correction or manipulation was performed. Where appropriate, aspect ratios of the high contrast images were determined from the ratio of the vertical (y) axis to the horizontal (x) axis (a_y/a_x) of an ellipse superimposed onto the droplet (see Fig. 2(a)).

In the optical tweezers setup, the custom-built trapping chamber was isolated by a cover slip (Chance Glass, #0 thickness) through which the objective focused the trapping beams. The traps were populated from the aerosol flow generated by an ultrasonic nebulizer (Omron NE U22) containing aqueous solutions of either sodium chloride (Sigma, 99.9999%) doped with a small amount of sodium dodecyl sulfate (Fisher, electrophoresis grade) or sucrose (Sigma, >99.5%). The relative humidity (RH) of the trapping chamber was controlled by varying the relative flow rates of dry and humidified nitrogen originating from the boil-off flow of a liquid N_2 dewar. The relative flow rates were controlled using paired mass flow controllers (Bronkhorst). The RH was measured at the outlet of the cell using a capacitance probe (Honeywell).

B. Simulations of droplet coalescence

A purpose-built finite-element-based computational code was used to capture the dynamics of the coalescence of two drops and their subsequent oscillations. The bulk flow of the liquid is governed by the incompressible Navier-Stokes equations with classical boundary conditions applied at the free-surface. The complexity of the problem is such that numerical methods are required.

The computational framework has already been used to probe the coalescence event in a series of articles that compare different models for the process,¹⁶ establish the influence of the surrounding gas,³⁶ study the inertia-dominated regime,³⁷ identify the dominant forces in the initial stages of coalescence,³⁸ and determine how coalescing drops can jump from superhydrophobic surfaces.³⁹ A full description of the models used, benchmark simulations confirming the code's accuracy, and a comparison to recent experimental data can be found in these papers. Furthermore, a step-by-step user-friendly guide to the development of the code can be found in Sprittles and Shikhmurzaev.⁴⁰ Therefore, here we only briefly recapitulate the main details.

The code uses an arbitrary Lagrangian Eulerian approach, so that the free surface dynamics are captured with high accuracy. The mesh is based on the bipolar coordinate system and is graded so that exceptionally small elements can be placed in the region where the two droplets first touch. Consequently, and in contrast to many previous works, both local and global physical scales of the coalescence process are properly resolved. Triangular-shaped finite elements of

V6P3 type are used, and the result of our spatial discretization is a system of non-linear differential algebraic equations of index two that are solved using the second-order backward differentiation formula (BDF2) using a time step which automatically adapts during a simulation to capture the appropriate temporal scale at that instant. The resulting equations are solved at each time step using a quasi-Newton method.

III. RESULTS AND DISCUSSION

The coalescence of picolitre-droplets across a range of different viscosities and compositions was studied. The experiments and simulations discussed in Secs. III A-III C are grouped according to the similarity in viscosity of the coalescing droplets as quantified by the Ohnesorge number, which relates the viscous forces to the inertial and surface tension forces in the droplets by the relation $Oh = \eta/(\rho\sigma a)^{1/2}$, where η is the droplet dynamic viscosity, ρ is the droplet density, σ is the droplet surface tension, and a is the droplet radius. If $Oh \lesssim 1$, inertial forces initially dominate viscous forces and coalescence takes the form of damped oscillations in droplet shape. If $Oh \gtrsim 1$, viscous forces are dominant and coalescence takes the form of a slow merging of the two precursor droplets.

A. Coalescence of like-viscosity droplets with $Oh < 1$

In the experiments described here, two optically trapped 6-10 μm radius droplets are brought close together to induce coalescence. In the limit of low viscosity,^{41,42} the droplet shape during and immediately after coalescence takes the form of a damped oscillator with the time-dependent amplitude $A(t)$ given by

$$A(t) = \sum_l A_{0,l} \exp\left(-\frac{t}{\tau_l}\right) \cos \omega_l t, \quad (1)$$

where

$$\tau_l = \frac{a^2 \rho}{(l-1)(2l+1)\eta} \quad (2)$$

and

$$\omega_l^2 = \frac{l(l-1)(l+2)\sigma}{a^3 \rho}. \quad (3)$$

In this equation, $A_{0,l}$ is the initial droplet amplitude for a mode order l (which corresponds to a characteristic deformation in droplet shape), τ_l is the characteristic damping (or relaxation) time for a given mode order, and ω_l is the angular oscillation frequency of a given mode order.

Accurate determination of properties such as droplet surface tension and viscosity relies critically on the ability to infer τ and ω from a coalescence experiment. However, owing to the small size and fast time scale of coalescing 6-10 μm droplets, τ and ω generally cannot be directly or precisely determined by imaging. Instead, they are inferred from the form of the EBL.^{8,11} Uncertainties arise about the impact of the initial position and orientation of droplets in the laser beam on EBL intensity. Implementation of a high frame rate

camera allows for the confident interpretation of the features present in the EBL and more accurate quantification of the droplet dynamics during the coalescence event.

Figures 2 and 3 present coalescence events for two sodium chloride droplets doped with the surfactant sodium dodecyl sulfate. Sodium chloride was used as the primary solute to reduce water activity below a value of 1, allowing for stable trapping and manipulation of the droplets.⁴³ These figures illustrate the processes occurring on the microsecond time scale around the coalescence event. Sequential images were captured with 8 μs exposure time, which required the region of interest for the camera sensor to be made very small (80×96 pixels). The droplets were doped with surfactant to decrease the surface tension and oscillation frequency (ω) and thereby facilitate the observation of shape distortions with the camera. In the example shown in Fig. 2, the pair of droplets were located at similar heights above the cover slip prior to the coalescence event, which subsequently occurred transverse to the trapping beams, whereas in Fig. 3, the relative strengths of the traps were adjusted such that droplets were located at different heights above the cover slip and coalescence occurred along an axis parallel to the trapping beams (axial coalescence).⁴⁴ Fig. 2(a) shows high frame rate images (8 μs time resolution) that clearly illustrate the damped oscillations in the droplet shape immediately after coalescence. Before time $t = 0$, the two trapped precursor droplets are visible at the top and bottom of the image. The full image of the precursor droplets is cropped as a result of the limited region of interest. After time $t = 0$, the composite droplet is observed to oscillate in shape, with the distortion decreasing with time until the droplet achieves a spherical shape at $t \approx 60 \mu\text{s}$. The progression in shape clearly indicates the dominance of the $l = 2$ oscillation mode (corresponding to alternating prolate and oblate distortions from a spherical geometry) in governing the shape during this time period. Additionally, the location of the composite droplet is at a position intermediate between the precursor droplets (i.e., approximately equidistant from the two optical traps). This position is dictated by the relative sizes of the precursor droplets.⁴⁵ The observed shift in droplet position away from both optical traps reinforces our previous conclusion that optical forces are much smaller than the capillary forces that drive the coalescence event.⁴⁶ Time-dependent aspect ratios (a_y/a_x) for the composite droplet shown in Fig. 2(a) are plotted in Fig. 2(b), clearly illustrating the damped oscillator form of the shape relaxation.

In addition to high frame rate imaging, the EBL measured by the oscilloscope for the same coalescence event is shown in Fig. 2(b). The oscilloscope provides a time resolution of ~ 100 ns, which is nearly a 2 orders of magnitude improvement over the resolution provided by the high frame rate camera. A correspondence is clear between the aspect ratio and EBL intensity. The EBL signal maxima correspond to frames from the high frame rate images in which the droplet is elongated along the y-axis (high aspect ratio), whereas the minima correspond to frames in which the droplet is elongated along the x-axis (low aspect ratio). Note that the optical traps are located at the top and bottom of the image, so a higher EBL intensity is expected for high aspect ratio droplets. The

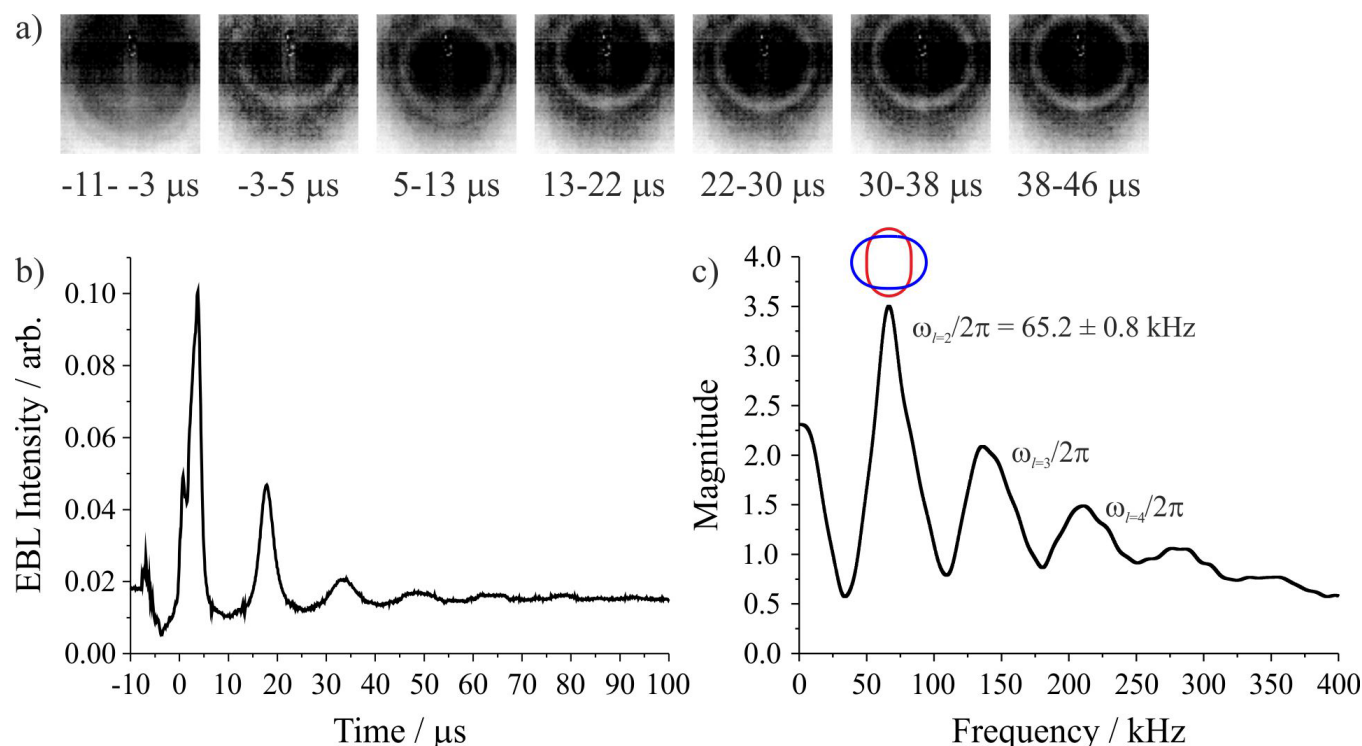


FIG. 3. Coalescence along an axis parallel to the trapping beam of two sodium chloride droplets doped with the surfactant sodium dodecyl sulfate. (a) High frame rate camera images of the coalescence event. Time ranges underneath each image provide the exposure period during which the image was taken. (b) EBL collected after coalescence (time $t = 0$ corresponds to the moment of coalescence). (c) Fast Fourier transform of the EBL gives the frequencies of the shape oscillations.

higher frequency features observed in the EBL arise from Fabry-Perot type interference resonances. The change in the optical path length of the trapping beam through the droplet as it oscillates in shape leads to modulation in the interference on backscattering with the direct reflection from the front face of the droplet.⁸ Figure 2(c) shows the fast Fourier transform of the EBL in Fig. 2(b), giving the frequency of the shape oscillation and confirming that the $l = 2$ mode is predominately excited upon coalescence. The broad, low intensity peaks at higher frequency correspond to the $l = 3$ and $l = 4$ modes.

Figure 3 presents a coalescence event where the precursor droplets initially have different heights above the cover slip. As a result, a droplet in one trap migrates onto the axis of the adjacent trapping beam and coalesces with the other droplet along an axis parallel to the trapping beam. The imaging plane is transverse to the optical trapping beam (and the collision geometry of the droplets) in the sequence of images shown in Fig. 3(a). Consequently the images do not illustrate the asymmetric changes in the droplet shape following coalescence. The asymmetrical shape distortion of the composite droplet (which was seen in the high frame rate images in Fig. 2(a)) occurs in vertical planes parallel to the beam axis. The shape distortion recorded in Fig. 3(a) is symmetrical with a periodically increasing and decreasing radius that is difficult to resolve from the camera images. Although the shape distortion is unclear in the experimental images, it is evident from the variation in EBL intensity in Fig. 3(b). Qualitatively there are many similarities to the trace shown in Fig. 2(b), most notably the periodic changes in intensity. However, there are two key differences. First,

there are fewer additional features in the EBL. This difference probably arises from the fact that, in this geometry, the coalesced droplet is entirely contained within one optical trap. Therefore, interference features present in the transverse coalescence geometry, which results in shape oscillations that intercept the light in both optical traps, are not present. Second, the fast Fourier transform of the EBL (Fig. 3(c)) shows that the magnitude of the $l = 2$ mode is decreased relative to that of the $l = 3$ and $l = 4$ modes (at higher frequencies). This difference is likely to be the result of the modest distortion in shape for the $l = 2$ mode perpendicular to the beam path for axial relative to transverse coalescence geometries. The observation of a coalescence event with an axial geometry enables the existence of higher order modes to be identified in the fast Fourier transform, which are not as clearly resolved in a measurement from a transverse geometry due to the dominance of the $l = 2$ mode and additional noise from the higher frequency interference features.

These experimental observations were confirmed by simulating the binary coalescence of droplets using the computational framework described earlier. The coalescence of two $8 \mu\text{m}$ radius droplets with $\eta = 1 \text{ mPa s}$, $\sigma = 72 \text{ mN m}^{-1}$, and $\rho = 1 \text{ g cm}^{-3}$ was examined, and animations showing the same coalescence simulation from two orthogonal perspectives are provided in videos 1 and 2 of the supplementary material.⁴⁷ If different assumptions for surface tension were made (e.g., using a value representative of a solution containing sodium dodecyl sulfate), the frequency of the shape oscillation would change, but the shape distortions observed in each plane would remain the same. Figure 4(a)

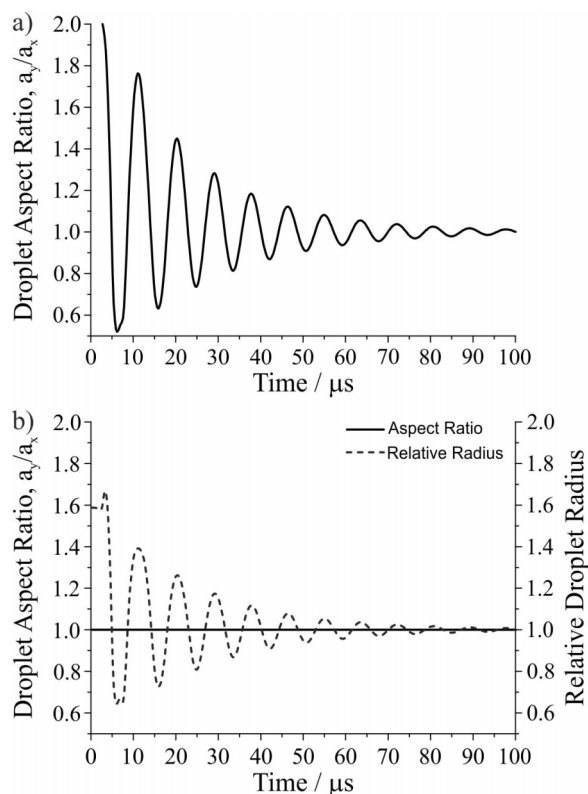


FIG. 4. Simulations of the coalescence of two $8\text{ }\mu\text{m}$ radius droplets examined (a) from a plane parallel to the axis of coalescence (analogous to the experimental observations shown in Fig. 2) and (b) from a plane transverse to the axis of coalescence (analogous to the experimental observations shown in Fig. 3). Time-dependent droplet aspect ratios are plotted in (a) and (b). Relative change in radius is plotted in (b). Simulated droplet properties are $\eta = 1 \times 10^{-3}\text{ Pa s}$, $\sigma = 72\text{ mN m}^{-1}$, and $\rho = 1\text{ g cm}^{-3}$.

shows the droplet aspect ratio from the simulated coalescence event viewed from a plane parallel to the axis of approach (analogous to the coalescence geometry in Fig. 2). From this perspective, the aspect ratios clearly follow the form of a damped oscillator and are similar to the observations from Fig. 2. Figure 4(b) shows the simulated aspect ratios and droplet radius relative to that of the composite droplet for the same coalescence viewed from a plane perpendicular to the axis of droplet approach (analogous to the coalescence geometry in Fig. 3). The droplet aspect ratio is equal to 1 and unchanging, with relatively minor changes in the relative droplet radius. These changes are consistent with the observations reported in Fig. 3 and corroborate our interpretation of the experimental data.

In addition to differences in processes occurring on the microsecond time scale, the coalescence geometry relative to the camera frame of reference also impacts observations on the millisecond time scale. Figure 5 presents the EBL with selected images showing processes occurring during the milliseconds before and after coalescence for transverse (Fig. 5(a)) and parallel (Fig. 5(b)) events. In both, the large spike in EBL at time $t = 0$ corresponds to the moment of coalescence and the initial shape distortion. For the transverse coalescence (Fig. 5(a)), a gradual decrease in EBL intensity is observed over the first 2 ms after the end of the shape oscillation (which occurs in between the two optical traps).

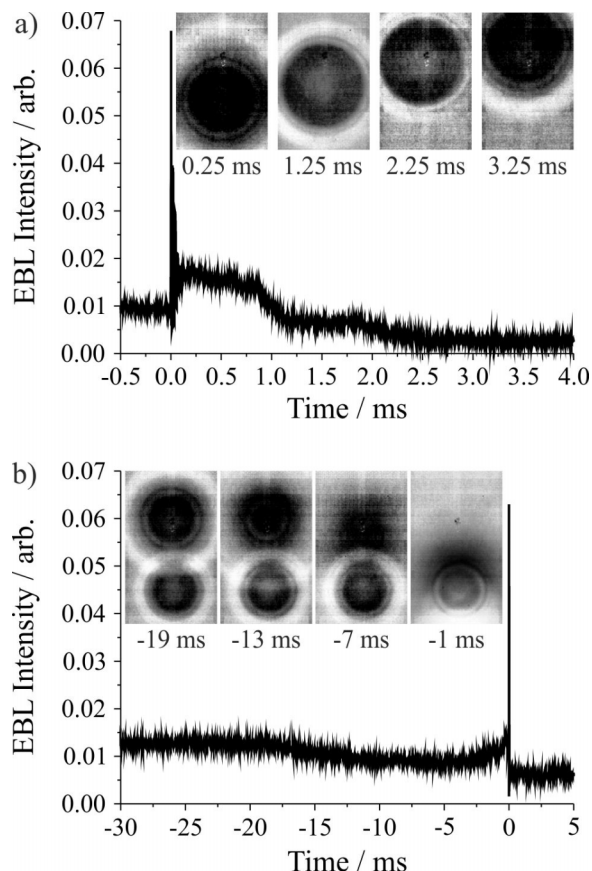


FIG. 5. Expanded view of the two coalescence events in Figs. 2 and 3 to show features of the EBL that occur on the millisecond time scale. (a) Coalescence transverse to the trapping beam. (b) Coalescence parallel to the trapping beam. Images at different moments during each coalescence are provided as insets.

From the high frame rate images (inset), it is clear that this gradual decrease results from the recapture of the coalesced droplet in one of the optical traps. On the other hand, for the coalescence occurring parallel to the trapping beam (Fig. 5(b)), the droplet coalescence occurs in one of the optical traps. A gradual shift in EBL intensity is not observed after coalescence because the coalescence occurs when both droplets are already confined within one of the optical traps. However, the EBL intensity changes before coalescence as a droplet is gradually pulled from one trap into the other, eventually inducing coalescence. This phenomenon is illustrated by the images in Fig. 5(b). At 19 ms before coalescence, two droplets are stably trapped. Over the intervening period until coalescence, the droplet located at a higher position is pulled into the axis of the adjacent laser beam, and just before coalescence, it is almost completely obscured by the other droplet located at the beam waist. The trajectory of this droplet gives rise to the slow changes in the EBL intensity before the coalescence event, similar to the previous observations of coalescence between a free-flowing and optically trapped droplet.³⁵

In short, the combination of high frame rate imaging and EBL allows a very precise understanding of the dynamics of coalescence. First, the combination of the two approaches shows that two time scales can be discriminated during coalescence in a dual optical trap. Shape distortion occurs

on the microsecond time scale. Migration of the coalesced droplet into one of the optical traps (coalescence transverse to the trapping beam) or of a precursor droplet from one trap to another (coalescence parallel to the trapping beam) occurs on the millisecond time scale. Understanding and distinguishing these two processes is essential to confidently identify which portion of the EBL is relevant to the coalescence event. Second, the coalescence geometry has an impact on the observed form of the EBL, and this arises due to the location of the coalescence event relative to the positions of the optical traps and the axis along which the shape distortion is viewed. Correctly assigning the origin of the key features in the EBL permits more confident determination of the oscillation frequency and relaxation time. As will be discussed next, a full understanding of droplet dynamics in the optical tweezers also allows for the evaluation of the range of experimental conditions where inferring relaxation time from the EBL is quantitatively appropriate.

B. Coalescence of like-viscosity droplets with $Oh > 1$

When $Oh > 1$, viscous forces dominate, the shape oscillations are efficiently damped, and only a slow merging of two droplets is observed during coalescence. In this case, the droplet shape relaxes to a sphere with a time constant⁴⁸

$$\tau_l = \frac{2(2l^2 + 4l + 3)a\eta}{l(l+2)(2l+1)\sigma}. \quad (4)$$

A straightforward method to determine the relaxation time constant is by imaging coalescing droplets and examining the time dependence of the aspect ratio of the relaxing composite droplet. Unfortunately, for droplets with radii on the order of micrometres and with viscosities near or a few orders of magnitude above the critical viscosity for efficient damping of surface oscillations, such a measurement is beyond the capabilities of most cameras as a time resolution on the order of $10 \mu\text{s}$ is required. Instead, the collection of EBL after coalescence is the only means to monitor (indirectly) the relaxation in droplet shape. However, as discussed previously, there are additional complications in the EBL, namely the additional interference features and the millisecond scale shifts in intensity due to rearrangement of the composite droplet position in the optical traps. A direct comparison of the EBL to high frame rate images allows the determination of whether these additional features to the EBL complicate precise quantification of the relaxation time constant.

Figure 6 shows coalescence events for sucrose droplets at three different RH values: 89%, 86%, and 82%. For each, the EBL is plotted as a function of time (left axis) along with the droplet aspect ratio from high frame rate imaging as a function of time (right axis). In addition, the experimental data were fit to an exponential decay using a non-linear least squares algorithm. Exponential fits to the EBL (dashed lines) and droplet aspect ratio (dotted lines) are given and the best fit values for the relaxation time constant for each are inset in the figure. The relaxation time constant and associated uncertainty reported for each fit were determined by systematically varying the initial time point included in

the least squares fit and taking the average and standard deviation of the best fits. To the top right side of each figure are a selection of high frame rate images taken during the relaxation period. To the bottom right side are the images of simulated droplets taken at the same time during the relaxation period (discussed in more detail later).

Figure 6(a) presents coalescence of sucrose at 89% RH, where the droplet has a viscosity (estimated at 90 mPa s) only slightly above the critical viscosity for efficient damping of the surface oscillations.¹¹ For this droplet, relaxation to a sphere is very fast, occurring within about $60 \mu\text{s}$ from coalescence. Indeed, relaxation occurs so quickly that even with a time resolution of $10 \mu\text{s}$, only 3-4 images showing a distorted droplet shape are captured. The EBL shows a clear initial increase (arising from increasing interception of the trapping beams by the surface area of the two droplets as they initially merge) followed by a rapid decrease in intensity that corresponds to the later stages of droplet relaxation to a sphere. Note that the maximum in EBL intensity corresponds to a maximum interception of the trapping beams by the distorted droplet surface area. The higher order features on the decreasing side of the EBL result as the optical path length through the composite droplet passes through resonant lengths typical of a Fabry-Perot type resonant form. Fitting exponential decays to both the EBL and the droplet aspect ratios gives a relaxation time constant of $13 \pm 1 \mu\text{s}$ from the EBL and $12 \pm 1 \mu\text{s}$ from the images, which is a remarkable agreement considering the additional features in the EBL and the small number of images captured during relaxation (along with the relatively wide time window for each image). The good agreement between the measured relaxation time constants indicates that both approaches are essentially equivalent.

Figure 6(b) shows the coalescence of sucrose droplets at 86% RH, which is considerably more viscous ($\eta_{\text{est}} = 350 \text{ mPa s}$). Note the change in time scale relative to Fig. 6(a). In this case, relaxation occurs over hundreds of microseconds and tens of images are recorded that show the relaxation in droplet shape. Again, for the EBL, the higher order features on the decreasing side of the trace correspond to a Fabry-Perot type resonant condition. Nonetheless, very good agreement exists between the relaxation time constants fit from the EBL ($52 \pm 4 \mu\text{s}$) and the droplet aspect ratios ($48 \pm 4 \mu\text{s}$).

Figure 6(c) shows the coalescence of sucrose droplets at 82% RH, which corresponds to droplets with a viscosity about an order of magnitude larger than those studied at 86% RH ($\eta_{\text{est}} = 6400 \text{ mPa s}$). In this case, relaxation occurs over several milliseconds, and it is clear that the agreement between the fit obtained from the EBL ($360 \pm 30 \mu\text{s}$) does not agree well with that obtained from the droplet aspect ratios ($870 \pm 60 \mu\text{s}$). The reason for this relates to the time scale of droplet recapture into the optical traps, which also occurs over milliseconds. As a result, two different processes are occurring that give a more complicated EBL, and separating them becomes quite challenging. The two processes are evident in the experimental images of Fig. 6(c). Initially (see image at $661\text{--}678 \mu\text{s}$) the newly coalesced droplet is located between the two optical traps, which are located at the top and bottom of the image.

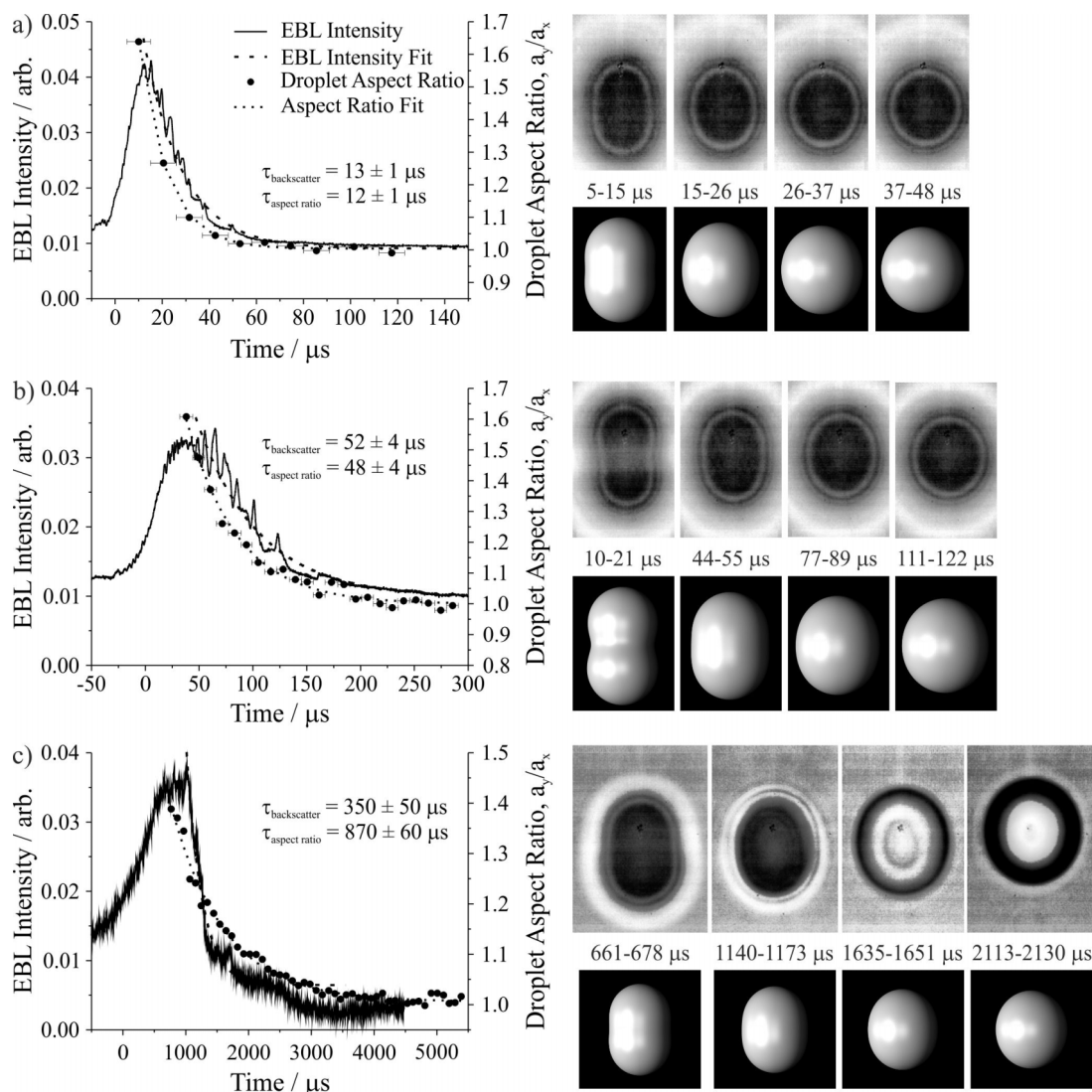


FIG. 6. Coalescence of sucrose droplets at (a) 89% RH ($\eta_{\text{est}} = 90$ mPa s), (b) 86% RH ($\eta_{\text{est}} = 350$ mPa s), and (c) 82% RH ($\eta_{\text{est}} = 6400$ mPa s). For each, the solid line represents the EBL and the dashed line represents the exponential fit to the EBL (left axis). The circles represent droplet aspect ratio and the dotted line gives the appropriate exponential fit (right axis). To the right of each plot are selected images during each coalescence event from both experiments (top) and simulations (bottom) with the appropriate times listed in between them. Note the different horizontal axis scales for each plot.

As the coalescence progresses, the droplet gradually relaxes to a sphere, but the droplet position shifts upwards over the same time period as it migrates to the upper trap (image at 2113-2130 μs). Although these are two relatively simple processes to distinguish in the images, they convolute the EBL, giving a relaxation time constant that is smaller than that determined from the droplet aspect ratios. In short, these observations indicate that once coalescence times last for more than a millisecond, EBL is no longer an effective approach to quantitatively infer changes in droplet shape.

In the experimental setup used here, the droplet radius was not directly measured, so it is not possible to precisely determine the droplet viscosity using Eq. (2) or (4). However, in a typical experiment, droplets are usually 6-10 μm in radius. Assuming the two precursor droplets are both 8 μm radius and droplet surface tension and density are equal to that of pure water (72 mN m^{-1} , 1 g cm^{-3}), the droplet viscosity can be estimated. Note that these are estimations but would likely be within approximately a factor of 2 of the true viscosity. We

used these approximate viscosities along with the assumed radius, surface tension, and density to simulate the expected droplet dynamics at those viscosities. The simulations were accomplished using the computational framework described earlier and provide a way to directly compare the experimentally observed aspect ratios to an idealized coalescence event for droplets of the same properties.¹⁶ Images of simulated droplets are provided below the images of experimentally observed droplets at the same time period after initial coalescence. Across all three experiments, there is a clear agreement between the experimental and simulated droplet shapes, providing confidence in the measurements. A more quantitative comparison between simulations and experiments is discussed next.

Figure 7 illustrates the time scales over which the droplet viscosity can be determined using both approaches simultaneously. Figure 7(a) shows the case of a low viscosity droplet ($\text{Oh} \ll 1$), where shape oscillations are evident. The circles represent droplet aspect ratio maxima derived from

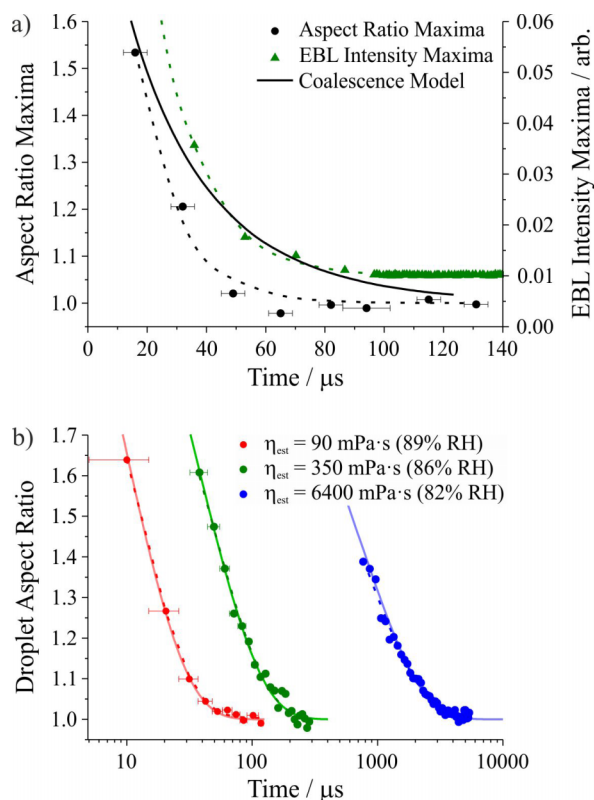


FIG. 7. Comparison of experiments and simulations for the coalescence of four different droplets. (a) Coalescence of the sodium dodecyl sulfate-doped sodium chloride droplets shown in Fig. 2 ($Oh \ll 1$). Circles represent droplet aspect ratio maxima (left axis) whereas triangles represent EBL maxima (right axis). The corresponding dotted line gives the exponential fit for each measurement. The solid line represents the simulated droplet aspect ratios. The estimated viscosity of the coalesced droplet is $0.67 \text{ mPa}\cdot\text{s}$. (b) Coalescence of the sucrose droplets shown in Fig. 6 ($Oh \gg 1$). Circles represent measured aspect ratios, dotted lines give the exponential fit to the measurement, and solid lines give the simulated aspect ratios. Note the logarithmic scale on the horizontal axis of part (b).

high frame rate images and the triangles represent the maxima in EBL intensity. The corresponding dotted lines give the best fit exponential decay to the experimental data. The solid line gives the simulation results. In Fig. 7(b) the circles represent droplet aspect ratios from the high frame rate imaging, dotted lines give the best fit exponential decay, and solid lines give the simulation results. Fig. 7(b) compares the relaxation time scales of all three droplets examined in Fig. 6. Figure 7 demonstrates that the time range required for droplet shape relaxation can span several orders of magnitude, even over a relatively small range in RH.

Droplet aspect ratios extracted from the simulated droplet shape are represented in Fig. 7 by the solid lines. Examples of the simulated droplet shape are given in Fig. 6. The simulated results are shifted in time to align with the experiments, as the moment of initial contact between the two precursor droplets does not necessarily correspond with the trigger threshold on the oscilloscope. A comparison of experimental and simulated droplet aspect ratios indicates that they agree well, validating the approach of using droplet aspect ratio to infer droplet relaxation time and indirectly validating (for lower viscosity droplets) the use of EBL to infer the relaxation time. For the lowest viscosity droplet (Fig. 7(a)), a minor disagreement

between the high frame rate images, EBL, and the simulation is evident, but in fact this disagreement is rather small. For the images, it arises from the rapid changes in droplet shape during the $\sim 8 \mu\text{s}$ period of exposure. For the EBL, the mismatch is much smaller and originates from broad maxima resulting from the interaction of the EBL from the two traps. Across all studied coalescence events, if additional processes were occurring in the droplet that impact the relaxation, the result would be a mismatch between simulation and experiment. Therefore, the agreement between the two indicates that the dynamics of coalescence are well understood for the precision required in these experiments.

C. Coalescence of dissimilar-viscosity droplets

The preceding discussion provides comparisons between simultaneous measurements of the EBL from coalescing droplets and high frame rate imaging and demonstrates that consistent information can be gained by both approaches. However, the EBL alone is not always sufficient to fully understand the coalescence event. As illustrated in the discussion of Fig. 6, if the coalescence time scale is of the same magnitude as the time scale for the composite droplet to migrate into one of the optical traps, then extraction of the coalescence time scale from the EBL becomes challenging and may indeed be ambiguous. Even more complex is the interpretation of the EBL during the coalescence of two droplets of different viscosities. Figure 8(a) shows an example of coalescence between two droplets of very different compositions and viscosities. Only images are shown because the EBL in this experiment is not informative. First, a sucrose solution was nebulized into the chamber to capture a sucrose droplet. Next, a sodium chloride solution was briefly nebulized into the chamber to capture a second droplet. As a result, the lower droplet in the image is composed of sucrose and a small amount of sodium chloride, whereas the upper droplet contains only sodium chloride. Both droplets were equilibrated to 55% RH and then coalesced, with the progress monitored by high frame rate imaging. Assuming binary component droplets containing one solute and water, the sodium chloride droplet is estimated to have a viscosity of $\sim 5 \times 10^{-3} \text{ Pa}\cdot\text{s}$ and the sucrose droplet a viscosity about $10^4 \text{ Pa}\cdot\text{s}$, a difference of about seven orders of magnitude. It is likely that the viscosity of the sucrose droplet is less than $10^4 \text{ Pa}\cdot\text{s}$ due to the addition of a small amount of sodium chloride while trapping the second droplet. Nonetheless, the viscosity can be expected to be far higher than for a pure sodium chloride droplet. For comparison, Fig. 8(b) shows the coalescence of two sodium chloride droplets equilibrated to 55% RH and Fig. 8(c) shows the coalescence of two sucrose droplets equilibrated to the same RH.

From Fig. 8(a), it is apparent that the coalescence of dissimilar viscosity droplets does not proceed in the same manner as coalescence of two droplets of similar chemical composition and viscosity. Initially, after coalescence, a composite droplet with a phase-separated structure is formed. As the coalescence progresses, the sucrose droplet (which does not contain much water) gradually dissolves into the sodium chloride droplet (which retains a substantial amount

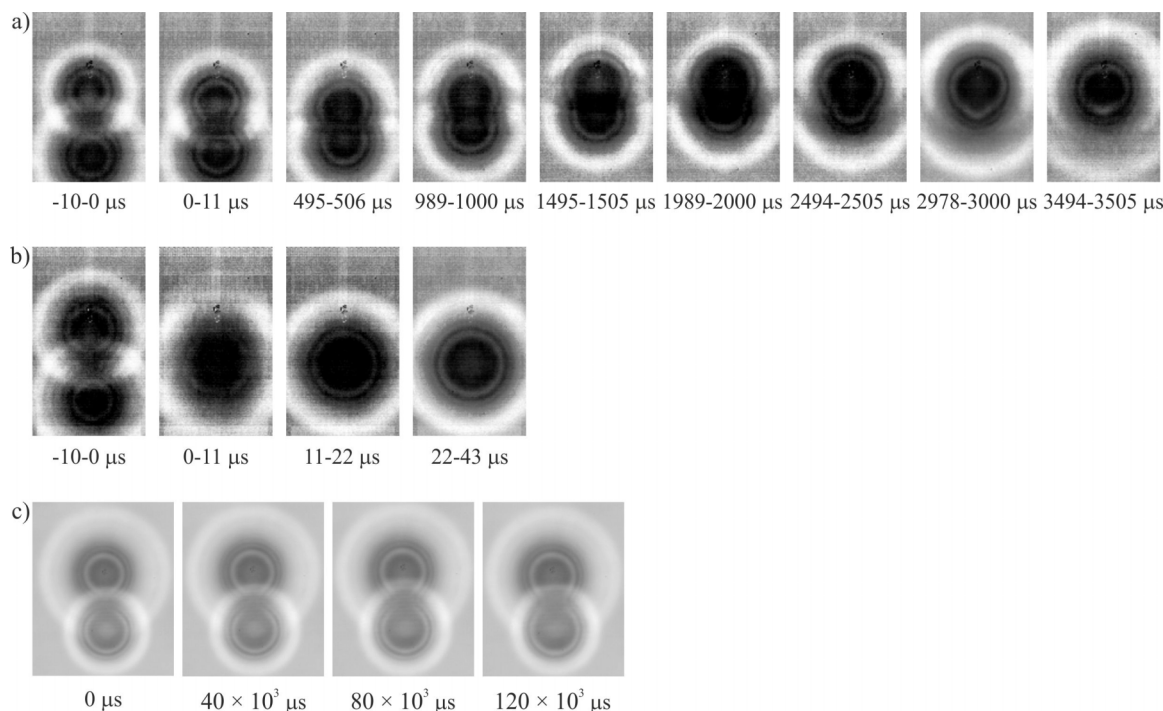


FIG. 8. Coalescence of droplets equilibrated to approximately 55% RH. (a) Coalescence of a sodium chloride droplet (top) and a sucrose droplet (bottom) results in the sucrose droplet dissolving in the sodium chloride droplet over about 3000 μs . (b) Two sodium chloride droplets coalesce quickly at the same RH. (c) Two sucrose droplets coalesce very slowly at the same RH. Note the different time scales for each coalescence event.

of water) until a fully coalesced, spherical droplet is formed after about 3000 μs . Note that the shift in the centre of mass of the coalescing droplets during the period of the coalescence is due to the recapture of the composite droplet into the upper optical trap. By contrast, the coalescence of two sodium chloride droplets at the same RH is complete within only a few microseconds (Fig. 8(b)), whereas the coalescence of two sucrose droplets at the same RH is very slow, with little observable progress over 120 000 μs (Fig. 8(c)). Instead, the time scale of coalescence more closely approximates that of sucrose equilibrated to 82% RH (Fig. 6(c)). This experiment demonstrates the potential for high frame rate imaging of coalescing droplets to enable quantification of dissolution kinetics, which are important to understanding powder properties,⁴⁹ coating qualities,⁵⁰ and cloud droplet formation.⁵¹ Moreover, high frame rate video imaging of the coalescence of particles that initially appear phase separated can give information about the transition to equilibrium morphology and allow the determination of properties such as the surface tension of the two initial droplets.^{14,52–54}

IV. CONCLUSIONS

In this work, the dynamics of droplet coalescence in a dual optical trap were investigated using a high frame rate camera capable of time resolution $<10 \mu\text{s}$, EBL from the trapping laser, and simulations of droplet coalescence dynamics. Examination of the coalescence dynamics of low viscosity droplets ($\eta \approx 10^{-3} \text{ Pa s}$, $\text{Oh} \ll 1$) simultaneously by both high frame rate imaging and EBL resolves key processes during coalescence. Coalescing droplets are pulled out of their respective optical traps at the moment of coalescence,

as capillary forces are much stronger than the traps' optical forces. Two processes occur on different time scales for low viscosity droplets: droplet shape distortion and relaxation to a sphere occurs on the microsecond time scale, whereas droplet migration into one of the optical traps occurs on the millisecond time scale. High frame rate imaging allows for clear delineation of these two processes and unequivocal assignment of the different observed features in the EBL. The specific geometry of the coalescence impacts the magnitude of the observed shape oscillation, which can be resolved through the EBL. For low viscosity droplets, this work validates the use of the EBL alone to precisely determine τ and ω when the time scale of coalescence is too fast for highly time-resolved monitoring by imaging. As droplets become more viscous ($\text{Oh} > 1$), the surface oscillations are immediately damped and coalescence is simply the merging of two droplets. We show that the relaxation time can be directly determined from the time-dependent change in droplet aspect ratio from the high frame rate images. Additionally, the relaxation can be inferred from the decay in the EBL. If relaxation is sufficiently fast ($\lesssim 2 \text{ ms}$), the two approaches are equivalent. However, if the droplet is sufficiently viscous (e.g., $\geq 1 \text{ Pa s}$), the convolution of the relaxation in droplet shape with recapture of the coalesced droplet into an optical trap hinders a quantitative determination of relaxation time by EBL. In these cases, droplet imaging provides a clearer, more quantitative approach. Simulations of droplet coalescence permitted validation of both approaches and showed that the fundamental physical processes during coalescence are well understood. This result indicates that the extracted relaxation times and oscillation frequencies using the holographic optical tweezers approach are robust and implies that the approach allows for straightforward determination

of both surface tension and viscosity. Lastly, study of the coalescence of dissimilar viscosity droplets highlights the time scale of transition to equilibrium shape and suggests that it may be possible to use holographic optical tweezers to elucidate dissolution kinetics.

ACKNOWLEDGMENTS

Jean-Pierre Wolf and Jérôme Kasparian are acknowledged for the loan of the high frame rate camera. J.P.R. and B.R.B. acknowledge support from the Engineering and Physical Sciences Research Council (EPSRC) through Grant No. EP/L010569/1. J.E.S. acknowledges support from EPSRC through Grant No. EP/N016602/1. The experimental and simulated data are provided through the University of Bristol data repository at J. P. Reid (2015), DOI: 10.5523/bris.1034k0rnvir0c1d6pphbas1sc1.

- ¹B. Croft, U. Lohmann, R. V. Martin, P. Stier, S. Wurzler, J. Feichter, R. Posselt, and S. Ferrachat, *Atmos. Chem. Phys.* **9**, 4653 (2009).
- ²K. Ardon-Dryer, Y. W. Huang, and D. J. Cziczo, *Atmos. Chem. Phys.* **15**, 9159 (2015).
- ³E. S. Robinson, R. Saleh, and N. M. Donahue, *J. Phys. Chem. A* **117**, 13935 (2013).
- ⁴J. R. Starr and B. J. Mason, *Q. J. R. Meteorol. Soc.* **92**, 490 (1966).
- ⁵G. D. Martin, S. D. Hoath, and I. M. Hutchings, *J. Phys.: Conf. Ser.* **105**, 012001 (2008).
- ⁶R. Vehring, W. R. Foss, and D. Lechuga-Ballesteros, *J. Aerosol Sci.* **38**, 728 (2007).
- ⁷J. W. Ivey, R. Vehring, and W. H. Finlay, *Expert Opin. Drug Delivery* **12**, 901 (2015).
- ⁸B. R. Bzdek, R. M. Power, S. H. Simpson, J. P. Reid, and C. P. Royall, *Chem. Sci.* **7**, 274 (2016).
- ⁹Y. Tian, R. G. Holt, and R. E. Apfel, *Rev. Sci. Instrum.* **66**, 3349 (1995).
- ¹⁰L. Yang, B. K. Kazmierski, S. D. Hoath, S. Jung, W.-K. Hsiao, Y. Wang, A. Berson, O. Harlen, N. Kapur, and C. D. Bain, *Phys. Fluids* **26**, 113103 (2014).
- ¹¹R. M. Power, S. H. Simpson, J. P. Reid, and A. J. Hudson, *Chem. Sci.* **4**, 2597 (2013).
- ¹²E. Bichoutskaia, A. L. Boatwright, A. Khachatourian, and A. J. Stace, *J. Chem. Phys.* **133**, 024105 (2010).
- ¹³R. M. Power, D. R. Burnham, and J. P. Reid, *Appl. Opt.* **53**, 8522 (2014).
- ¹⁴Y. Qiu and V. Molinero, *J. Am. Chem. Soc.* **137**, 10642 (2015).
- ¹⁵H. Pathak, A. Obeidat, G. Wilemski, and B. Wyslouzil, *J. Chem. Phys.* **140**, 224318 (2014).
- ¹⁶J. E. Sprittles and Y. D. Shikhmurzaev, *Phys. Fluids* **24**, 122105 (2012).
- ¹⁷D. Aarts, H. N. W. Lekkerkerker, H. Guo, G. H. Wegdam, and D. Bonn, *Phys. Rev. Lett.* **95**, 164503 (2005).
- ¹⁸Y. Chen, C. Shen, and G. P. Peterson, *Ind. Eng. Chem. Res.* **54**, 9257 (2015).
- ¹⁹M. M. Wu, T. Cubaud, and C. M. Ho, *Phys. Fluids* **16**, L51 (2004).
- ²⁰S. W. Wilkins, T. E. Gureyev, D. Gao, A. Pogany, and A. W. Stevenson, *Nature* **384**, 335 (1996).
- ²¹K. Fezzaa and Y. Wang, *Phys. Rev. Lett.* **100**, 104501 (2008).
- ²²S. C. Case, *Phys. Rev. E* **79**, 026307 (2009).
- ²³S. C. Case and S. R. Nagel, *Phys. Rev. Lett.* **100**, 084503 (2008).
- ²⁴J. D. Paulsen, J. C. Burton, and S. R. Nagel, *Phys. Rev. Lett.* **106**, 114501 (2011).
- ²⁵J.-Y. Kohno, M. Kobayashi, and T. Suzuki, *Chem. Phys. Lett.* **578**, 15 (2013).
- ²⁶Y. Takano, S. Kikkawa, T. Suzuki, and J.-Y. Kohno, *J. Phys. Chem. B* **119**, 7062 (2015).
- ²⁷T. Suzuki and J.-Y. Kohno, *J. Phys. Chem. B* **118**, 5781 (2014).
- ²⁸R. M. Power and J. P. Reid, *Rep. Prog. Phys.* **77**, 074601 (2014).
- ²⁹J. Buajarern, L. Mitchem, A. D. Ward, N. H. Nahler, D. McGloin, and J. P. Reid, *J. Chem. Phys.* **125**, 114506 (2006).
- ³⁰J. R. Butler, J. B. Wills, L. Mitchem, D. R. Burnham, D. McGloin, and J. P. Reid, *Lab Chip* **9**, 521 (2009).
- ³¹L. Mitchem, J. Buajarern, A. D. Ward, and J. P. Reid, *J. Phys. Chem. B* **110**, 13700 (2006).
- ³²L. Mitchem, R. J. Hopkins, J. Buajarern, A. D. Ward, and J. P. Reid, *Chem. Phys. Lett.* **432**, 362 (2006).
- ³³J. B. Wills, J. R. Butler, J. Palmer, and J. P. Reid, *Phys. Chem. Chem. Phys.* **11**, 8015 (2009).
- ³⁴J. B. Wills, K. J. Knox, and J. P. Reid, *Chem. Phys. Lett.* **481**, 153 (2009).
- ³⁵R. Power, J. P. Reid, S. Anand, D. McGloin, A. Almohamed, N. S. Mistry, and A. J. Hudson, *J. Phys. Chem. A* **116**, 8873 (2012).
- ³⁶J. E. Sprittles and Y. D. Shikhmurzaev, *J. Fluid Mech.* **751**, 480 (2014).
- ³⁷J. E. Sprittles and Y. D. Shikhmurzaev, *Phys. Rev. E* **89**, 063008 (2014).
- ³⁸J. E. Sprittles and Y. D. Shikhmurzaev, *J. Fluid Mech.* **753**, 279 (2014).
- ³⁹R. Enright, N. Miljkovic, J. Sprittles, K. Nolan, R. Mitchell, and E. N. Wang, *ACS Nano* **8**, 10352 (2014).
- ⁴⁰J. E. Sprittles and Y. D. Shikhmurzaev, *Int. J. Numer. Methods Fluids* **68**, 1257 (2012).
- ⁴¹H. Lamb, *Hydrodynamics*, 6th ed. (Cambridge University Press, Cambridge, 1932).
- ⁴²L. Rayleigh, *Proc. R. Soc. London* **29**, 71 (1879).
- ⁴³J. Buajarern, L. Mitchem, and J. P. Reid, *J. Phys. Chem. A* **111**, 13038 (2007).
- ⁴⁴K. J. Knox, D. R. Burnham, L. I. McCann, S. L. Murphy, D. McGloin, and J. P. Reid, *J. Opt. Soc. Am. B* **27**, 582 (2010).
- ⁴⁵B. M. Weon and J. H. Je, *Phys. Rev. Lett.* **108**, 224501 (2012).
- ⁴⁶A. D. Ward, M. G. Berry, C. D. Mellor, and C. D. Bain, *Chem. Commun.* **2006**, 4515.
- ⁴⁷See supplementary material at <http://dx.doi.org/10.1063/1.4959901> for supplementary videos 1 and 2, which show simulations of binary coalescence from two orthogonal perspectives.
- ⁴⁸S. Chandrasekhar, *Proc. London Math. Soc.* **3-9**, 141 (1959).
- ⁴⁹A. Marabi, G. Mayor, A. Burbidge, R. Wallach, and I. S. Saguy, *Chem. Eng. J.* **139**, 118 (2008).
- ⁵⁰A. van Kampen, B. Hitzmann, and R. Kohlus, *Powder Technol.* **286**, 325 (2015).
- ⁵¹A. Asa-Awuku and A. Nenes, *J. Geophys. Res.: Atmos.* **112**, D22201, doi:10.1029/2005JD006934 (2007).
- ⁵²B. J. Dennis-Smith, K. L. Hanford, N.-O. A. Kwamena, R. E. H. Miles, and J. P. Reid, *J. Phys. Chem. A* **116**, 6159 (2012).
- ⁵³N. O. A. Kwamena, J. Buajarern, and J. P. Reid, *J. Phys. Chem. A* **114**, 5787 (2010).
- ⁵⁴J. P. Reid, B. J. Dennis-Smith, N.-O. A. Kwamena, R. E. H. Miles, K. L. Hanford, and C. J. Homer, *Phys. Chem. Chem. Phys.* **13**, 15559 (2011).